Wave propagation and power deposition in magnetically enhanced inductively coupled and helicon plasma sources

Ronald L. Kinder[a] and Mark J. Kushner[b]
Department of Electrical and Computer Engineering, University of Illinois, 1406 West Green Street, Urbana, Illinois 61801

(Received 20 July 2000; accepted 2 October 2000)

Magnetically enhanced inductively coupled plasma (MEICP) and helicon sources for materials processing are of interest because of their ability to deposit power within the volume of the plasma beyond the classical skin depth. The location and manner of power deposition can vary substantially depending on the mode of operation and reactor conditions. The coupling of electromagnetic fields to the plasma typically occurs through two channels; a weakly damped heliconlike wave that penetrates into the bulk plasma and an electrostatic wave. The electrostatic wave can often be suppressed resulting in the helicon component being responsible for the majority of the power deposition. A computational investigation was conducted to quantify this heating and determine the conditions for which power can be deposited in the downstream region of MEICP devices. For typical process conditions (10 mTorr, 1 kW ICP) and magnetic fields above 40 G, radial and axial electric fields exhibit nodal structure consistent with helicon behavior. As the magnetic fields are increased, axial standing wave patterns occur with substantial power deposition downstream. The ability to deposit power downstream with increasing B field is ultimately limited by the increasing wavelength. For example, if the plasma is significantly electronegative in the low power–high magnetic field regime, power deposition resembles conventional ICP due to the helicon wavelength exceeding the reactor. [DOI: 10.1116/1.1329122]

I. INTRODUCTION

As the semiconductor industry transitions to larger wafer sizes ($\geqslant$300 mm) plasma sources which are capable of maintaining process uniformity over large areas will be required. Magnetically enhanced inductively coupled plasma (MEICP) and helicon sources have been proposed as possible alternatives to conventional inductively coupled plasma (ICP) sources due to their high ionization efficiency and their ability to deposit power within the volume of the plasma.[1–3] Operation of MEICP and helicon sources at low magnetic fields ($<$100 G) is not only economically attractive, but may enable greater ion flux uniformity to the substrate than high magnetic field devices such as electron cyclotron resonance sources since ions are only moderately magnetized.

Chen and Boswell, and Cheetham and Rayner have identified several modes of operation for MEICPs,[4–9] summarized as electrostatic, inductive, helicon, and high pressure helicon modes.[8,9] In the inductive mode fields are evanescent and decrease in amplitude with a classical skin depth, whereas the helicon mode consists of low frequency whistler waves occurring in that region where the electromagnetic frequency, ω, lies between the lower hybrid frequency and the electron cyclotron frequency, ω_{ce}, and well below the plasma frequency.[10] Degeling and Boswell have suggested that the transition from an ICP to a helicon mode occurs as a result of a positive feedback as the skin depth decreases to the scale length of the system.[11]

MEICPs typically have a higher plasma density for a given power deposition than ICP sources. Landau damping has been proposed as one mechanism through which more efficient heating may occur.[12] In this process, energetic primary electrons are produced through trapping and acceleration by a helicon wave. The electrons produce ionization, lowering their energy and generating a low energy secondary. The wave reaccelerates electrons after each ionization event. Scharer and Gui found that trapped electrons appear as the magnetic field amplitude increases, and that the electron energy distribution has a bunching of particles with energies higher than the ionization energy of the gas.[13] Recent measurements of the phase of the optical emission from high-lying short-lived excited states of Ar^+ showed them to be well correlated with the phase velocity of the helicon wave.[14] Blackwell *et al.*, however, have recently found that there may be too few phased fast electrons to account for a major portion of the ionization to occur through Landau damping.[15] More recently, Kwak suggested that much of the electron heating comes from an electrostatic component of the helicon wave.[16]

When a finite electron mass is taken into account in a cold plasma model another solution to the wave equation appears in bounded geometries at frequencies above the lower hybrid. This is referred to as the electrostatic Trivelpiece–Gould (TG) and was identified by Trivelpiece and Gould as the cavity eigenmode of a cold plasma, space charge wave in a cylinder.[17] In unbounded plasmas these waves are commonly referred to as whistler waves. The TG mode has been observed in plasmas at high ratios of wave frequency $\omega/\omega_{ce} \approx 0.1-2.0$. Being nearly electrostatic and of short radial wavelength, these waves are strongly absorbed as they

[a]Electronic mail: r-kinder@uiuc.edu
[b]Electronic mail: mjk@uiuc.edu

propagate perpendicular to the externally applied static magnetic field lines. In this regard, it has been suggested that helicon waves deposit power by coupling to TG waves at the radial boundary, which are then rapidly absorbed.[18] Chen *et al.* proposed that this mechanism, rather than Landau damping, accounts for the efficiency of helicon sources.[19] Borg and Boswell have suggested that the TG mode may enhance wave damping in the presence of high electron collision rates due to a high electric field amplitude near the location of resonant power flux.[20]

One common characteristic feature of many MEICP and helicon devices is their ability to produce a maximum plasma density in the downstream region of processing chambers (remote from the antenna), which implies that substantial power deposition also occurs downstream.[21] Strongly damped electrostatic TG waves can reach the plasma core at low magnetic fields, while at high fields they deposit power at the periphery of the plasma column. For conditions where the TG wave is suppressed the helicon component deposits the majority of the power within the plasma volume. The collisional damping of helicon waves is weak and propagation along the external static magnetic field lines can occur under many experimental conditions.[18] Such propagation may allow for power deposition to occur in the downstream region of MEICP devices.

To investigate the coupling of the electromagnetic radiation to the plasma in MEICPs, algorithms were developed for wave propagation in the presence of static magnetic fields using the two-dimensional Hybrid Plasma Equipment Model (HPEM).[22–24] A full tensor conductivity was added to the electromagnetic module, which enables one to calculate three-dimensional components of the inductively coupled electric field based on two-dimensional applied magnetostatic fields. Electromagnetic fields were obtained by solving the wave equation where plasma neutrality was enforced. By neglecting the divergence term in the solution of Maxwell's equations the effects of the TG mode on plasma heating are ignored. The purpose of these investigations was to determine the effect of helicon heating and the ability to deposit power in the downstream region of helicon devices. An effective collision frequency for Landau damping was also included and is most influential in the low electron density or high magnetic field regimes. However, it was observed that it only has a minimal effect on power deposition efficiency. Results for an argon plasma excited by an $m=0$ mode field at 13.65 MHz show a resonant peak in the plasma density occurring at low magnetic fields which is attributed to off-resonant cyclotron heating. At higher magnetic fields (>150 G), radial and axial electric fields exhibit downstream wave patterns consistent with helicon behavior. The results agree with experiments in which the plasma density increases as the magnetic field is increased, an effect attributed to the onset of a propagating helicon wave or to a change in the helicon wave eigenmode.[25] The transition from inductive coupling to helicon mode appears to occur when the fraction of the power deposited through radial and axial fields dominates. The model will be described in Sec. II, followed by a discussion of our results in Secs. III–V. Concluding remarks are in Sec. VI.

II. DESCRIPTION OF THE MODEL

Algorithms were developed to enable investigations of MEICP tools using the HPEM. The HPEM has previously been described in detail, and will only briefly be discussed here.[22–24] The HPEM is a two-dimensional, plasma equipment model which consists of the Electromagnetic Module (EMM), the Electron Energy Transport Module (EETM), and the Fluid Kinetics Simulation (FKS). Electromagnetic fields and corresponding phases are calculated in the EMM. These fields are used in the EETM to solve the electron energy conservation equation to generate sources for electron impact processes and electron transport coefficients. These parameters are transferred to the FKS where momentum, continuity and energy equations are solved for all heavy particles. A drift diffusion formulation is used for electrons to enable an implicit solution of Poisson's equation for the electric potential. The species' densities and electrostatic fields produced in the FKS are transferred to the EETM and the EMM. These modules are iterated until a converged solution is obtained. The options used in the HPEM are continuity, momentum, and energy equations for all neutral and charged heavy particles. The electron energy equation was solved to obtain the electron temperature.

The EMM portion of the plasma model was improved to resolve three-dimensional components of the inductively coupled electric field based on two-dimensional applied magnetostatic fields and the azimuthal antenna currents. The results discussed here are for a two-dimensional (2D) (r,z) azimuthally symmetric geometry. The fluid equations for continuity, and momentum and energy transport are therefore solved in two dimensions. However, given azimuthal antenna currents and (r,z) magnetostatic fields, all three components of the inductively coupled electric field (r,θ,z) are generated, and we therefore solve for these three components. Local power deposition is computed in 2D from $P(\vec{r})=\vec{J}\cdot\vec{E}$, $\vec{J}=\bar{\bar{\sigma}}\cdot\vec{E}$, where $\vec{J}$, $\bar{\sigma}$, $\vec{E}$ are the three-dimensional current density, tensor conductivity (see the following), and electric field. This 2D power deposition is then used in the electron energy equation to obtain the electron temperature, source functions, and transport coefficients.

Assuming that $\nabla\cdot\mathbf{E}=0$, Maxwell's equations can be reduced to the conventional wave equation where the electric field, $\mathbf{E}$, is given in the frequency domain as

$$\nabla\cdot\frac{1}{\mu}\nabla\mathbf{E}+\omega^2\epsilon^2\mathbf{E}=i\omega\mathbf{J}, \tag{1}$$

where $\mathbf{J}$, ω, μ_0, and ϵ are, respectively, the current density, frequency, permeability, and permittivity. By setting $\nabla\cdot\vec{E}=0$, we ignore the consequences of the electrostatic TG mode on plasma heating. The focus of this study is to investigate the propagation and coupling mechanisms of the helicon component of the wave. In work to be reported elsewhere, we have included the electrostatic component in the

wave equation by approximating $\nabla \cdot \vec{E} = \Delta\rho/\epsilon_0$, where $\Delta\rho$ is a harmonically driven perturbation. The results of that study indicate that the effect of the TG mode is to restructure the power deposition profile near the coils. However, the propagation of the helicon component is little affected, particularly at large magnetic fields where the TG mode is damped. The results presented here are therefore most uncertain at low magnetic fields.

The current density has contributions from both the external antenna current and the conduction current generated in the plasma due to the electromagnetic wave. The conduction current is addressed by a cold plasma tensor,

$$\mathbf{J} = \bar{\bar{\sigma}} \cdot \mathbf{E} \tag{2}$$

with

$$\bar{\bar{\sigma}} = \frac{q n_e}{\alpha} \frac{1}{\alpha^2 + |\mathbf{B}|^2} \begin{pmatrix} \alpha^2 + B_r^2 & \alpha B_z + B_r B_\theta & -\alpha B_\theta + B_r B_z \\ -\alpha B_z + B_r B_\theta & \alpha^2 + B_\theta^2 & \alpha B_r + B_\theta B_z \\ \alpha B_\theta + B_r B_z & -\alpha B_r + B_\theta B_z & \alpha^2 + B_z^2 \end{pmatrix} \tag{3}$$

and

$$\alpha = \frac{m_e}{q}(\nu_e + i\omega), \tag{4}$$

where $\bar{\bar{\sigma}}$, q, n_e, $\mathbf{B}$, B_r, B_θ, B_z, m_e, and ν_e are, respectively, the conductivity tensor, electron charge, electron density, magnetic field, radial, azimuthal and axial magnetic field components, electron mass, and effective electron momentum transfer collision frequency. An analogous full tensor mobility is used for electron transport in the EETM and FKS, as described below. The ion current in solution of Eq. (1) is ignored due to the low mobility of ions. $\mathbf{E}(r)$ is obtained from the solution of Eq. (1), using a sparse matrix conjugate gradient method.[26]

The effective electron collision frequency includes a term for Landau damping, ν_{LD}, as described by Chen,[27]

$$\nu_{\mathrm{LD}} = 4\pi f \sqrt{\pi} \zeta^3 \exp(-\zeta^2), \tag{5}$$

where

$$\zeta = \sqrt{\frac{|\mathbf{B}| m_e \omega}{2 q^2 \mu_0 n_e T_e}}. \tag{6}$$

Here, T_e is the electron temperature. For $\zeta \gg 1$, ν_{LD} increases with increasing electron density at a constant magnetic field. However, in typical helicon sources where ζ may be less than unity, ν_{LD} can decrease with increasing electron density. The effective electron collision frequency is then the sum of the conventional momentum transfer collision frequency, ν_m, and the effective frequency for Landau damping, $\nu_e = \nu_m + \nu_{\mathrm{LD}}$.

The fluid continuity, momentum, and energy equations are time integrated in the FKS to provide species densities, fluxes, and temperatures, and Poisson's equation is solved for the electrostatic potential. Electron transport coefficients and electron impact sources are obtained from the EETM. The species densities are derived from the continuity equation,

$$\frac{\partial N_i}{\partial t} = -\nabla \cdot \Gamma_i + S_i, \tag{7}$$

where N_i, Γ_i, and S_i are the species density, flux, and source for species i. The flux for electrons is obtained using a drift-diffusion formulation to enable a semi-implicit solution of Poisson's equation, described below. The electron flux is given by

$$\overline{\Gamma_{\mathbf{e}}} = \bar{\bar{\mu}}_e \cdot \left(q_e N_e \overline{E_s} - \frac{k T_e}{|q_e|} \nabla N_e \right), \tag{8}$$

where $\bar{\bar{\mu}}_e$ is the electron tensor mobility having a form analogous to Eq. (3), T_e is the electron temperature and E_s is the electrostatic field. Fluxes for heavy particles (neutrals and ions) are individually obtained from their momentum equations

$$\frac{\partial \Gamma_i}{\partial t} = -\frac{1}{m_i}\nabla(N_i k T_i) - \nabla \cdot (N_i \overline{v_i} \overline{v_i}) + \frac{q_i}{m_i} N_i (\overline{E_s} + \overline{v_i} \times \overline{B}) - \nabla \cdot \bar{\bar{\mu}}_i - \sum_j \frac{m_j}{m_i + m_j} N_i N_j (\overline{v_i} - \overline{v_j}) \nu_{ij}, \tag{9}$$

where T_i is the temperature, q_i is the charge, $\overline{v_i}$ is velocity, $\bar{\bar{\mu}}_i$ is the viscosity tensor (used only for neutral species), and ν_{ij} is the collision frequency between species i and species j. The heavy particle temperature is determined by solving the energy equation,

$$\frac{\partial (N_i c_i T_i)}{\partial t} = \nabla \cdot \kappa_i \nabla T_i - P_i \nabla \cdot \overline{v_i} - \nabla \cdot (N_i \overline{v_i} \varepsilon_i) + \frac{N_i q_i^2 \nu_i}{m_i(\nu_i^2 + \omega^2)} E^2 + \frac{N_i q_i^2}{m_i \nu_i} E_s^2 + \sum_j 3 \frac{m_{ij}}{m_i + m_j} N_i N_j \nu_{ij} k_B (T_j - T_i) \pm \sum_j 3 N_i N_j R_{ij} k_B T_j, \tag{10}$$

where c_i is the heat capacity, κ_i is the thermal conductivity, P_i is the partial pressure, and R_{ij} is rate coefficient for formation of the species by collisions between heavy particles.

There are heating contributions for charged particles from both the electrostatic and electromagnetic fields.

The electrostatic field is obtained from a semi-implicit solution of Poisson's equation. The potential for use at time $t+\Delta t$, Φ, is obtained from an estimate of the charge density at that time which consists of the charge density ρ_0 at time t, incremented by the integral of the divergence of fluxes and sources over the next time interval,

$$-\nabla\cdot\epsilon\nabla\Phi=\rho_0+\Delta t\frac{d\rho}{dt}=\rho_0-\Delta t\sum_i q_i\nabla\cdot\Gamma_i$$
$$-\Delta t q_e\nabla\cdot\left(\bar{\bar{\mu}}_e\cdot\left(-q_e n_e\nabla\Phi-\frac{kT_e}{|q|}\nabla n_e\right)\right)$$
$$+\Delta t\sum_i q_i S_i. \tag{11}$$

The first sum is over the divergence of ion fluxes [as obtained from Eq. (9)]. The following term accounts for the electron flux and contains the potential, thereby providing the implicitness. The last term accounts for independent sources of charge which result from processes such as collisions, photoionization, secondary electron emission or electron beam injection. Equation (11) is solved using the method of successive-over-relaxation.

III. PROPAGATION IN A SOLENOIDAL GEOMETRY

Since helicon sources can have complex geometries, a solenoidal reactor was first used as a demonstration platform and to provide validation. This geometry is schematically shown in Fig. 1. The reactor is powered by a set of ring coils that are driven at 13.56 MHz with currents 180° out of phase. Process gas is injected at the top of a quartz tubular reactor through a shower head nozzle and flows out a pump port located at the bottom. The reactor sits inside a solenoidal magnetic field having dominantly an axial component with larger radial gradients near the ends of the solenoid. The base case has operating conditions of Ar gas at 10 mTorr, 50 sccm, and a power deposition of 1 kW. The collisional processes included in the model are ionization, excitation, and momentum transfer between electrons and neutral particles, Coulomb collisions between electrons and ions, charge exchange collisions between ions and neutral particles, and momentum transfer collisions among neutral particles. A listing of these reactions is in Ref. 28.

The spatially dependent plasma properties are a sensitive function of magnetic field strength and configuration. For example, azimuthal electric field amplitudes and phases are shown in Fig. 1 for magnetic field intensities of 10–150 G. At 10 G the azimuthal electric field peaks near the coils at 15 V/cm and remains in an inductively coupled mode where the amplitude decreases evanescently and is limited by the conventional plasma skin depth. The phase distributions show a radially inward traveling wave. (Wave propagation is perpendicular to the phase fronts.) As the magnetic field is increased, further penetration of the azimuthal electric field into the plasma occurs. Once the fields encounter a boundary

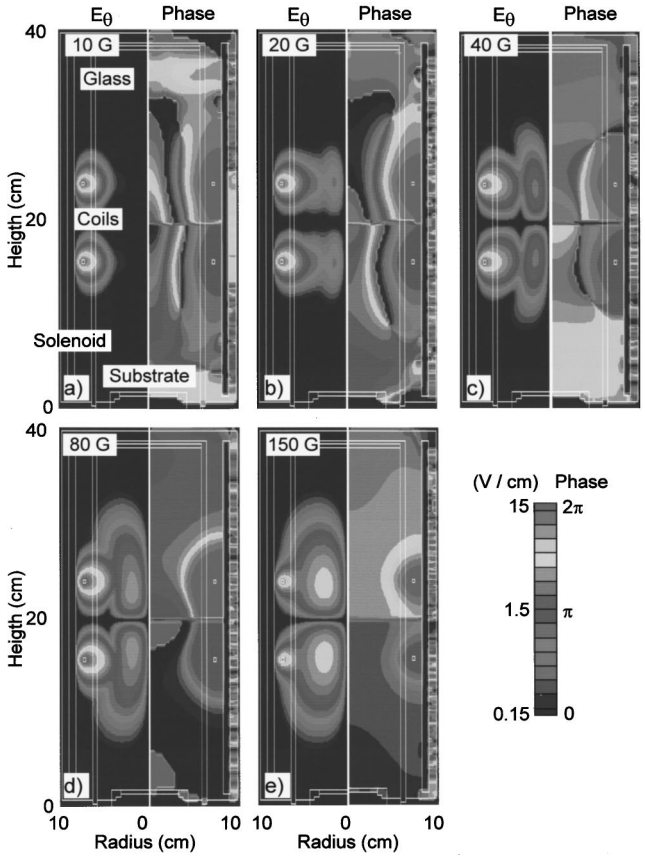

FIG. 1. Azimuthal electric field amplitude and corresponding phase in solenoidal geometry for (a) 10, (b) 20, (c) 40, (d) 80, and (e) 150 G. The process conditions are Ar, 10 mTorr, 1 kW power deposition. Increasing magnetic field produces propagation in the axial direction.

or a counterpropagating wave, a standing wave begins to form. At 40 G, a node appears in the azimuthal field while propagation begins to occur in the axial direction with an increasing axial wavelength. At 150 G there is a standing wave pattern in the radial direction with a peak midway between the coil and the axis of symmetry. As the static magnetic fields further increase, axial propagation of the electromagnetic fields dominates and the wavelength increases.

The radial electric fields over the same range of magnetic fields are shown in Fig. 2. At 10 G, the radial electric field has weak penetration into the plasma with there being a local maximum close to the coils and a node on the axis of symmetry. As the magnetic field is increased, further penetration occurs and a second local maximum in the radial electric field develops, indicating the onset of a standing wave in the radial direction. As the magnetic field is increased further, the amplitude of the second peak increases, while that of the first peak decreases. By 80 G, the first peak dissipates. At 10 G, propagation is dominantly in the radial direction and is highly damped. As the static magnetic field is increased, propagation changes from dominantly radial to dominantly axial, while the radial electric field wavelength increases proportionally. The axial electric field, shown in Fig. 3, behaves similarly. Note that the axial electric field intensity is two orders of magnitude smaller than the radial electric field due

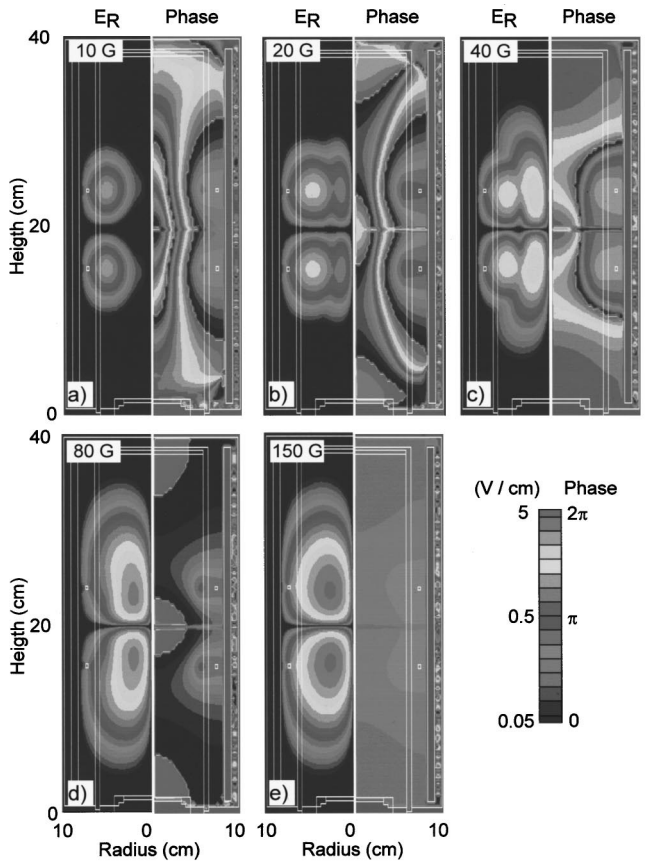

FIG. 2. Radial electric field amplitude and corresponding phase in solenoidal geometry for (a) 10, (b) 20, (c) 40, (d) 80, and (e) 150 G. The process conditions are Ar, 10 mTorr, 1 kW power deposition. Increasing magnetic field produces radial components of the electric field and propagation in the axial direction.

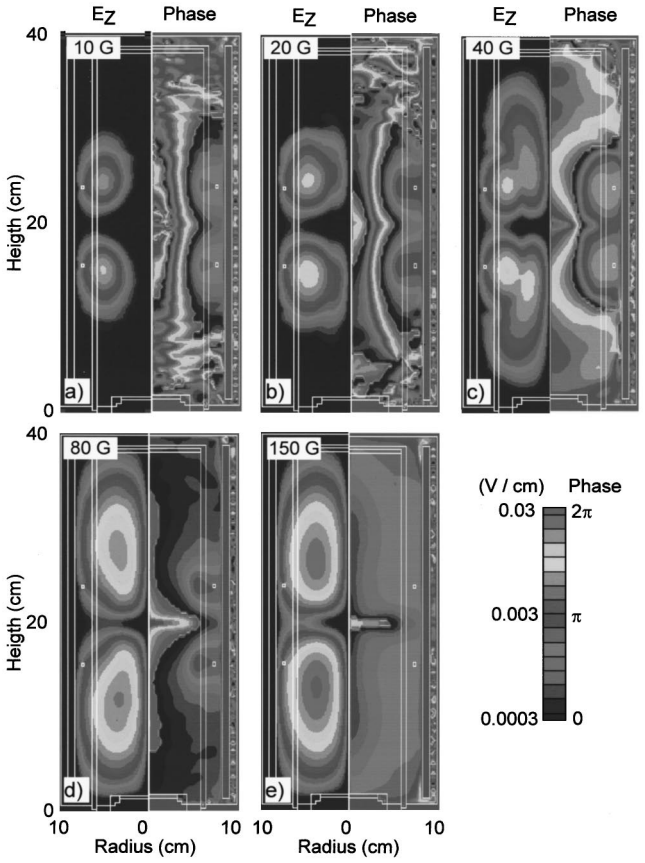

FIG. 3. Axial electric field amplitude and corresponding phase in solenoidal geometry for (a) 10, (b) 20, (c) 40, (d) 80, and (e) 150 G. The process conditions are Ar, 10 mTorr, 1 kW power deposition.

to the smaller magnetic field gradients in the radial direction compared to the axial direction.

The wavelength of the electromagnetic wave can be estimated from the phase diagrams of Figs. 1–3. The axial wavelength as a function of static magnetic field divided by the average electron density, $\beta = B/n_e$, for several tube radii are shown in Fig. 4(a). For a magnetic field of 40 G, electron density of $10^{11}\,\mathrm{cm}^{-3}$, and tube radius of 6 cm, the axial wavelength is approximately 10 cm. As the magnetic field increases or the electron density decreases, the axial wavelength increases. Similarly the axial wavelength increases with a decrease in tube radius. These results can be numerically fitted for the axial wavelength, λ_z, as

$$\lambda_z(\mathrm{cm}) = \frac{7.6\times 10^6}{R(\mathrm{cm})}\left(\frac{B(\mathrm{G})}{n_e(\mathrm{cm}^{-3})}\right)^{0.63}, \tag{12}$$

where R is the radius of the tube. Using the dispersion relation for a helicon wave, an estimate of the dependence of wavelength on plasma parameters can be obtained.[27] The axial wave number, k_z, is proportional to the total wave number, k, through the following dispersion relation:

$$k k_z = \omega q \mu_0 \frac{n_e}{B}. \tag{13}$$

For an $m=0$ mode, the radial wave number, $k_\perp$, is fixed by the tube radius,

$$k_\perp = \frac{3.83}{R}, \tag{14}$$

while the total wave number is defined by

$$k_\perp^2 + k_z^2 = k^2. \tag{15}$$

The theoretical axial wavelength for an $m=0$ mode obtained by substituting Eqs. (14) and (15) into Eq. (13) is shown in Fig. 4(b) as a function β for several tube radii. The computed axial wavelength is roughly 2/3 of the theoretical, most likely because of the mixed mode nature of the computed wave and the finite axial extent of the plasma.

IV. PLASMA HEATING AND POWER DEPOSITION

Power deposition and electron density are shown in Fig. 5 for different solenoidal magnetic fields. At 10 G, the electric fields are still predominantly inductively coupled, with power deposition occurring near the coils with a classical skin depth limited by the plasma conductivity. As the magnetic field is increased, the power deposition penetrates further into the volume of the plasma, in accordance with the electric fields shown in Figs. 1–3. At 40 G, the power deposition displays nodal behavior reflecting the shorter wave-

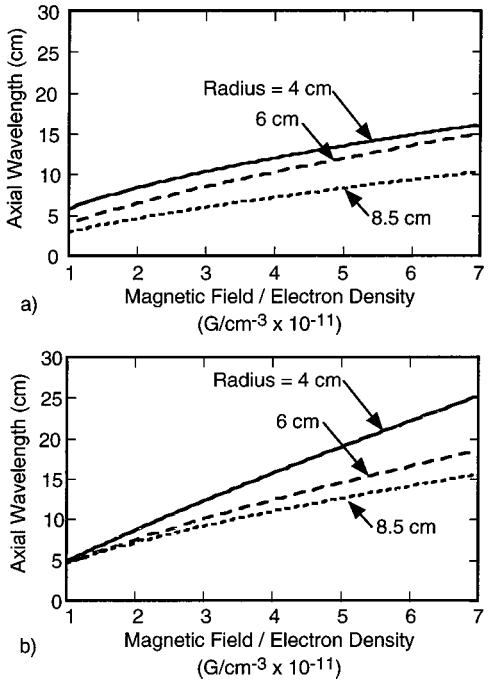

FIG. 4. Axial wavelength of the electromagnetic field as a function of static magnetic field divided by electron density. (a) Theoretical value from dispersion relation of an $m=0$ mode. (b) Computed value from simulations. The computed axial wavelength resembles that of an $m=0$ mode.

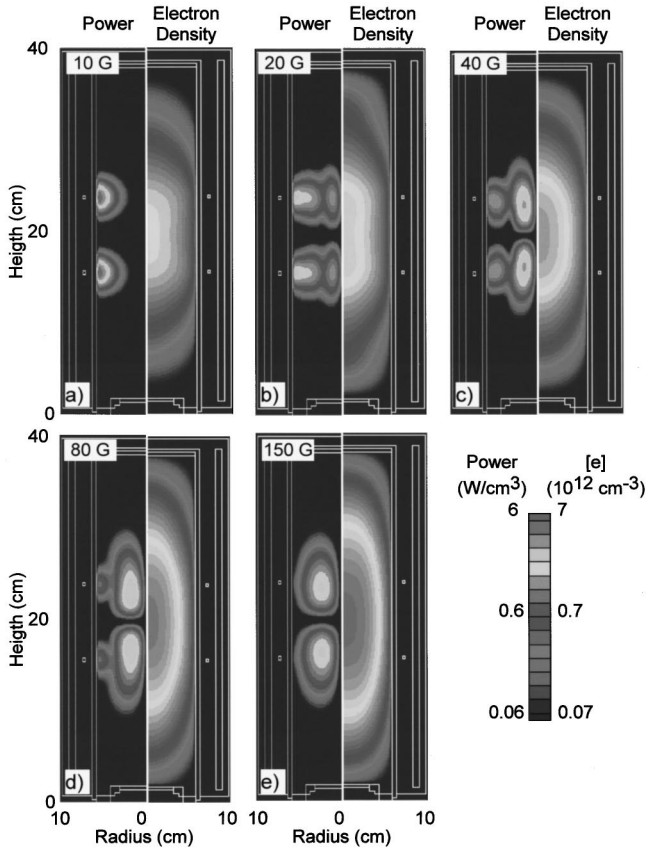

FIG. 5. Power deposition and electron density in solenoidal geometry for (a) 10, (b) 20, (c) 40, (d) 80, and (e) 150 G. The process conditions are Ar, 10 mTorr, 1 kW power deposition.

lengths of the azimuthal and radial electric fields. In all cases power deposition is off axis. The electron density is maximum on axis in the low magnetic field regime. As the magnetic field is increased the electron density increases, reflecting a decrease in radial diffusion losses. At fields larger than 150 G, the electron density is maximum off axis at the location of maximum power deposition.

Measurements by Chen and Decker showed a peak in the plasma density in the low magnetic field regime (20–60 G).[29] This peak was attributed to an electron cyclotron resonance (ECR), where the incident electromagnetic frequency is of the order of the electron cyclotron frequency. Simulations of this low magnetic field regime also produced a resonant peak in the plasma density in the downstream region, as shown in Fig. 6. This local maximum shifts toward higher magnetic fields as the radius of the tube is decreased. The maxima are similarly attributed to ''off-resonant'' electron cyclotron heating. The shift of the peak to higher magnetic field results from a shift in the efficiency of depositing power to a higher magnetic field as the effective electron collision frequency is increased. Normalized power deposition, $P=\mathrm{Re}[\mathbf{J}\cdot\mathbf{E}^*]$, as a function of magnetic field for several electron collision frequencies is shown in Fig. 7(a) for a plasma density of $10^{12}\,\mathrm{cm}^{-3}$ and $\omega/2\pi=13.56\,\mathrm{MHz}$. At $\nu_e=10^7\,\mathrm{s}^{-1}$, the normalized power deposition has a resonant peak occurring at around $B=15\,\mathrm{G}$. As the effective collision frequency increases, the width of the power deposition increases and the peak value decreases, while shifting the maximum toward higher magnetic fields. At $\nu_e=10^8\,\mathrm{s}^{-1}$, the normalized power deposition maximum has shifted to ~30 G. In a typical microwave ECR, operating at 2.45 GHz, the electron momentum transfer collision frequency is significantly smaller than the incident electromagnetic frequency and this off-resonant shift is unnoticeable. However, in a rf system the collision frequency is of the order of the incident electromagnetic frequency, thereby affecting the magnetic field at resonance and hence the location of the ECR zone. As the tube radius is decreased the local maximum in electron density at low magnetic field shifts toward higher magnetic fields, as shown in Fig. 6. The collision frequency in-

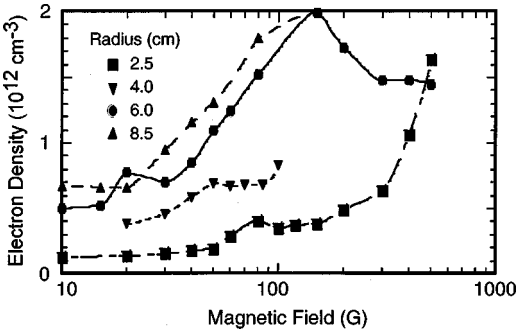

FIG. 6. On-axis value of electron density at $z=8$ cm for several tube radii as a function of static magnetic field in solenoidal geometry. Peaks at low magnetic field are attributed to off-resonance cyclotron heating.

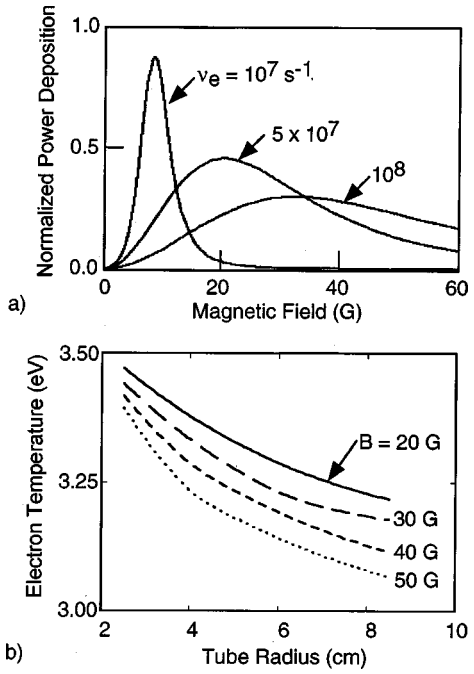

FIG. 7. Power deposition and electron temperature in the solenoidal geometry. (a) Normalized power deposition ($P = \mathbf{J}\cdot\mathbf{E}^*$) as a function of magnetic field for several values of the effective electron collision frequency. (b) Average electron temperature as a function of tube radius for varying magnetic field. The increase in the electron temperature with decreasing magnetic field produces a shift in the resonant magnetic field.

creases due to an increase in electron temperature as the tube radius decreases, as shown in Fig. 7(b).

The consequences of including collisional Landau damping on the electron density are shown in Fig. 8. The Landau damping term accounts for at most 15% of the total collision frequency. The Landau damping term has a peak near $\beta = 10^{10}\,\mathrm{cm}^{-3}\,\mathrm{G}^{-1}$ and has an approximate full width at half-maximum of $\beta = 2\times10^{10}\,\mathrm{cm}^{-3}\,\mathrm{G}^{-1}$. In the low electron density or high magnetic field regimes, the increase in the effective collision frequency due to Landau damping can shift the position of the peak power deposition (ECR resonance) to higher magnetic fields. For example, the peak in the electron density at low magnetic fields is removed when Landau damping is taken into account, as shown in Fig. 8.

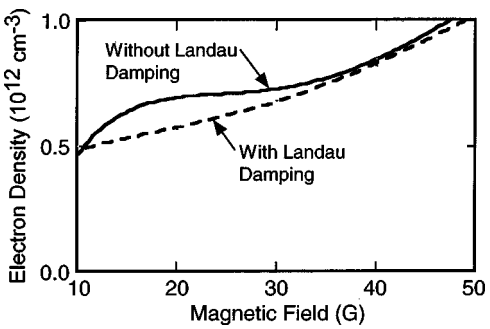

FIG. 8. On-axis value of electron density at $z = 10$ cm as a function of static magnetic field in solenoidal geometry with and without the collisional Landau damping term.

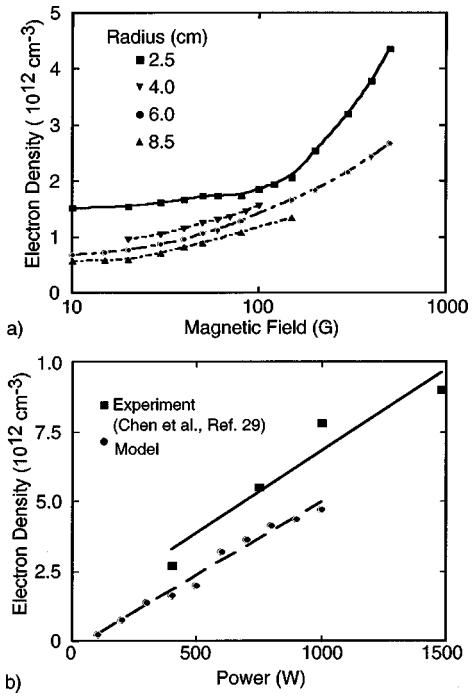

FIG. 9. Electron density in the solenoidal geometry. (a) Average electron density as a function of static magnetic field for several tube radii. (b) Experimental and computed average electron densities.

The reactor averaged electron density as a function of magnetic field is shown in Fig. 9(a). In the low magnetic field regime (<20 G), the electromagnetic fields are inductively coupled. There is no significant change in the electron density as the magnetic field is increased. At 20–60 G, ECR heating begins to contribute and the electron density increases. As the magnetic field is further increased the power deposited through the radial electric field begins to be com-

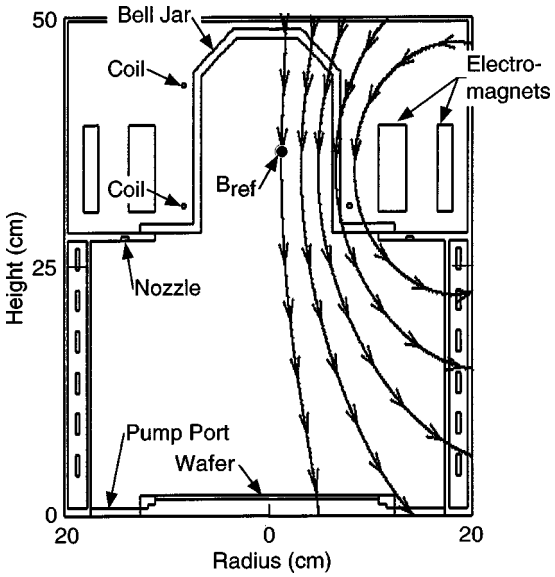

FIG. 10. Schematic of the Trikon helicon plasma source. Streamlines represent magnetic flux lines in the reactor. Location of the reference magnetic field point is in the bell jar.

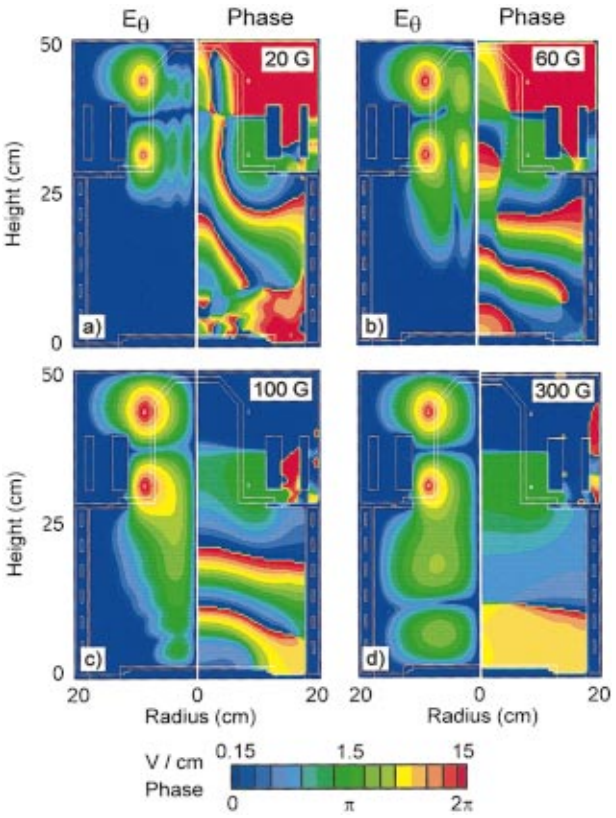

FIG. 11. Azimuthal electric field amplitude and corresponding phase in the Trikon tool for (a) 20, (b) 60, (c) 100, and (d) 300 G for an Ar plasma. Increasing magnetic field produces axial propagating waves.

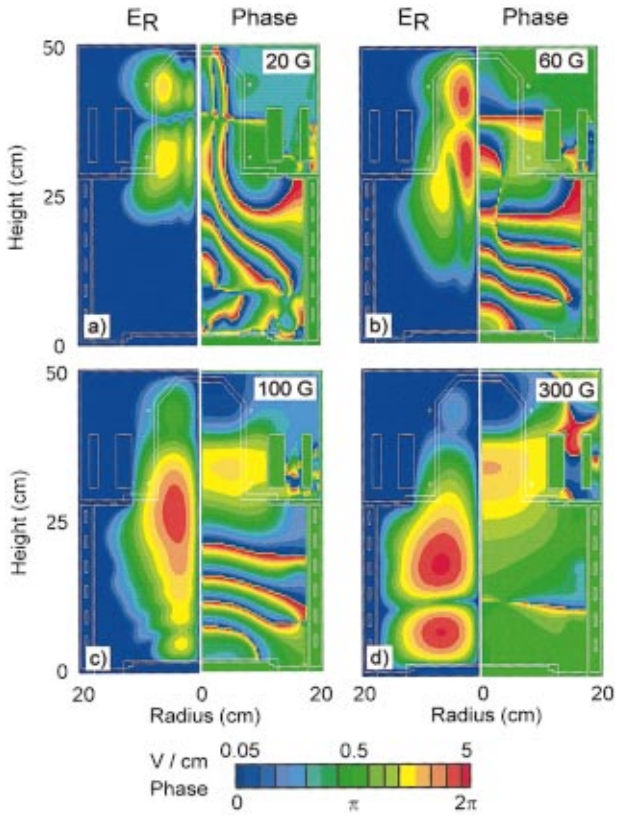

FIG. 12. Radial electric field amplitude and corresponding phase in the Trikon tool for (a) 20, (b) 60, (c) 100, and (d) 300 G for an Ar plasma.

parable to the power deposited through the azimuthal electric field. Power deposition through the radial electric fields increases due to the higher order standing wave pattern. At higher magnetic fields, it is expected that standing wave patterns with even higher order may appear as eigenvalue solutions for the radial electric field. Perry and Boswell showed that the electron density increases in ''jumps'' as the magnetic field and power are increased.[1,2] Each density step may be attributed to the onset of a higher order standing wave structure. Our simulations to date have not been able to resolve ''jumps'' in plasma density as a function of power when considering reactor averaged densities. For example, the electron density as function of incident power, shown in Fig. 9(b), is linear with power, in agreement with experiments by Chen *et al.*[29]

V. PLASMA PROPERTIES OF A HELICON PLASMA SOURCE

Simulations were also conducted in a geometry based on the Trikon Technologies, Inc., Pinnacle 8000 helicon plasma source, schematically shown in Fig. 10. Processing gas is injected through a nozzle located below the electromagnets and is exhausted through a pump port located around the outside diameter of the substrate. The quartz bell jar is surrounded by electromagnets which produce a solenoidal magnetic field inside the bell jar with flaring field lines in the downstream chamber region, as shown on the right-hand side of Fig. 10. The system is powered by two ring coils surrounding the bell jar. Each coil operates at 13.56 MHz and are 180° out of phase. Base case results have operating conditions of Ar gas at 10 mTorr, 50 sccm, and a power deposition of 1 kW.

Parametric studies were conducted while varying the magnetic field intensity. The cited magnetic fields are for an on-axis location midway between the antennas shown in Fig. 10. Azimuthal electric field amplitudes and phases are shown in Fig. 11 for magnetic fields of 20–300 G. For $B=20$ G, the azimuthal electric field is inductively coupled with the amplitude decreasing evanescently and being limited by the conventional plasma skin depth, as shown in Fig. 11(a). Similar to the results for the solenoidal reactor, the phase distributions show that a radial traveling wave dominates the propagation of the electromagnetic fields through the bell jar region and away from the coil. As the magnetic field is increased, further penetration of the azimuthal electric field into the plasma occurs. However, as radial penetration increases, axial conductivity increases, thereby allowing the azimuthal electric field to propagate downstream, as shown for $B=100$ G. When the propagating wave encounters a boundary, a standing wave pattern of the azimuthal field in the axial direction begins to form. At 300 G, Fig. 11(d), there is an off-axis downstream peak in the electric field. The propagation of the electric field in the axial direction begins to dominate concurrent with an increase in the wavelength. The distribution and propagation of the radial and axial elec-

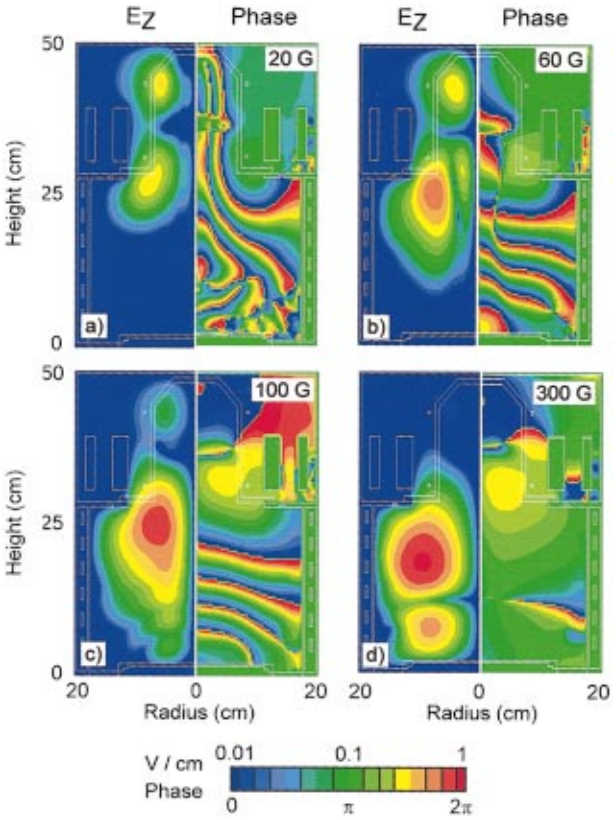

FIG. 13. Axial electric field amplitude and corresponding phase in the Trikon tool for (a) 20, (b) 60, (c) 100, and (d) 300 G for an Ar plasma.

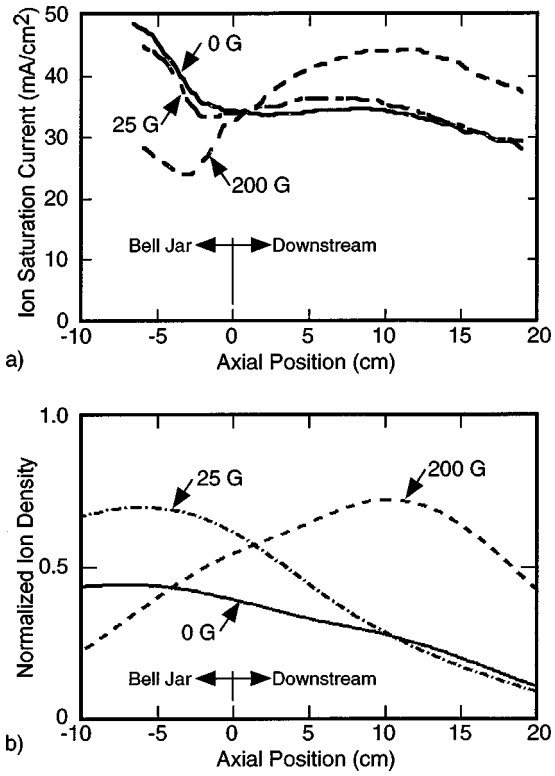

FIG. 14. Plasma properties as a function of axial location. (a) Experimental ion saturation current for several values of the static magnetic field. (b) Computed values of the normalized ion density. When increasing the magnetic field, the peak in the plasma density shifts from the bell jar to downstream.

tric fields, shown in Figs. 12 and 13, follow a similar pattern. Initially, inductive coupling dominates in the low magnetic field regime. Once the magnetic field is high enough (>100 G), downstream standing wave patterns appear and electromagnetic propagation in the axial direction dominates. Note that the magnitude of the radial and axial fields are of the same order, due to the diverging magnetic field lines which produce similar gradients in the radial and axial directions.

Experimental results for the axial ion saturation in the Trikon tool are shown in Fig. 14(a).[30] At low static magnetic fields, the ion saturation current peaks in the bell jar region of the reactor. As the magnetic fields are increased the peak in the ion saturation current and plasma density shift downstream. The calculated ion densities follow similar trends, shown in Fig. 14(b).

The electron density and power deposition are shown in Fig. 15. Power deposition follows the electric field profiles in the reactor. At 20 G, the power deposition peaks near the coils. As the magnetic fields are increased, there are nodal peaks in the electric field in the downstream region of the reactor, thereby depositing most of the power in the downstream region. This shift in the power deposition produces a shift in the peak plasma density to the downstream chamber. An off-axis peak in the plasma density can be maintained at such low pressures because of the high magnetic field which inhibits radial diffusion. The shift in power deposition increases the ion flux to the substrate while, for this example, decreasing uniformity.

Simulations were also conducted using an Ar/Cl_2 $=80/20$ gas mixture at 10 mTorr. The reaction chemistry for this case is listed in Ref. 28. This chemistry produces a large Cl^- negative ion density which significantly affects the power deposition and plasma distribution. The power deposition and corresponding electron density for varying magnetic fields are shown in Fig. 16. As with pure Ar, at low magnetic fields coupling is conventional ICP and most of the power deposition and the peak plasma density occur in the bell jar. As the magnetic field is increased, propagation of the electromagnetic fields tends to follow magnetic fields lines. The wavelength of the heliconlike wave increases along the direction of propagation and a nodal structure in the electromagnetic fields develops. At 150 G most of the power is deposited in the downstream region of the reactor. As the static magnetic field is further increased, the power deposition shifts back to the bell jar region as does the peak in plasma density. At 300 G the peak in the power deposition and ion density again occur in the bell jar region. This shift upstream occurs because of the increase in the wavelength of the heliconlike wave as the static magnetic field is increased. At a high enough magnetic field, the wavelength is too large to sustain a standing wave pattern inside the chamber.

The wavelength of the propagating wave is proportional to the magnitude of the static magnetic field and inversely proportional to the electron density. Noting that $\beta = B/n_e$ and $\lambda_z \sim \beta$, β is computed as a function of magnetic field

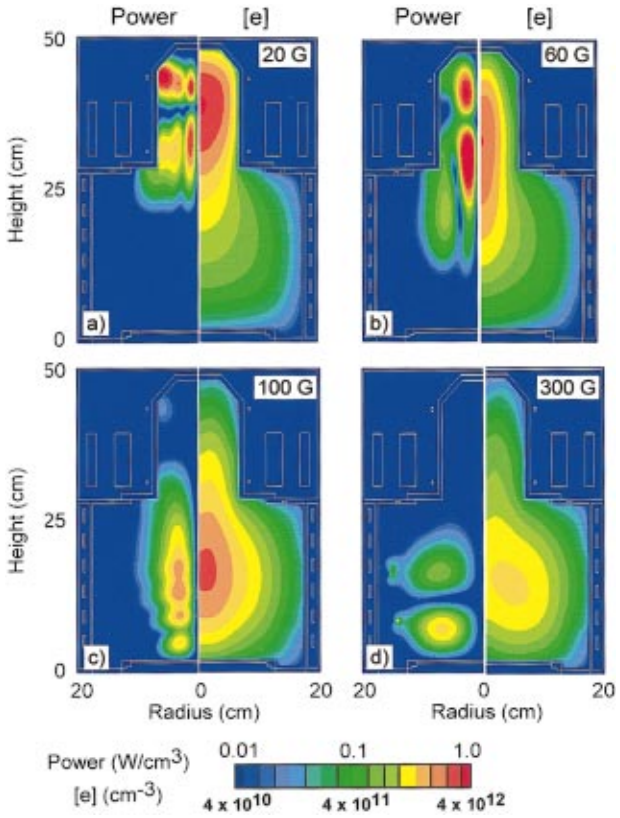

FIG. 15. Power deposition and electron density in the Trikon tool for (a) 20, (b) 60, (c) 100, and (d) 300 G for an Ar plasma. Increasing magnetic field produces a downstream plasma source.

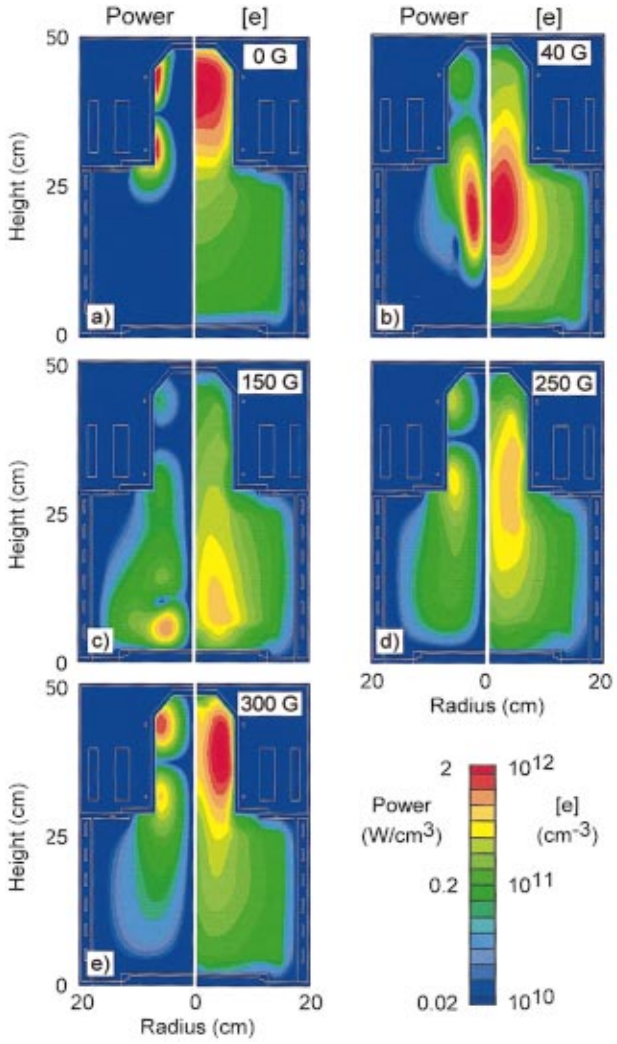

FIG. 16. Power deposition and electron density in the Trikon tool using an $Ar/Cl_2 = 80/20$ mixture for (a) 0, (b) 40, (c) 150, (d) 250, and (e) 300 G. At high magnetic field, the plasma density reverts to the bell jar due to the axial wavelength exceeding the reactor dimensions.

and power are shown in Fig. 17(a). The electron density for the calculation of β was at the reference location of the magnetic field. At low power, the electron density is low due to both a low ionization rate and a high rate of attachment to Cl_2. As the power increases, the Cl_2 is more heavily dissociated resulting in a lowering of the rate of attachment and increase in plasma density. In the low magnetic field–high power deposition regime β is small and the axial wavelength is shorter than the chamber dimensions allowing standing waves to occur. However, as the deposition power is decreased, β and the wavelength increase. Likewise as the magnetic field is increased, there is an increase in β and the wavelength. In the high magnetic field–low power regime, the wavelength is larger than the dimensions of the chamber. Unable to sustain a standing wave pattern, power deposition occurs near the coils in what resembles an inductively coupled mode.

The change in power deposition downstream, which occurs as a result of changing the mode of operation, clearly affects system performance such as uniformity and magnitude of reactive fluxes. Although the goal of this study was not to optimize system performance such as the uniformity of ion flux, it is nevertheless instructive to briefly examine such dependence. For example, the consequences of power deposition and magnetic field on the uniformity of the ion flux to the substrate for the conditions of Fig. 17(a) were quantified, using as a metric $U = 100 \cdot (\max - \min)/(\max + \min)$, where max/min are the maximum/minimum values of ion flux to the substrate. The results are shown in Fig. 17(b). For a region of operation having wavelength of 10–75 cm, U is largest, meaning less uniform. These conditions correspond to where there is significant electric field propagation downstream and the power deposition occurs directly above the substrate. Longer and shorter wavelengths have power deposition more remote from the substrate, thereby allowing diffusion to help homogenize the fluxes.

VI. CONCLUDING REMARKS

Power deposition in MEICP sources was investigated using a 2D plasma equipment model. The purpose of these investigations was to determine the consequences of helicon heating and the ability to deposit power in the downstream region of MEICP devices. 3D electromagnetic fields were obtained from 2D magnetostatic fields by solving the wave equation with a tensor conductivity using a sparse matrix conjugate gradient method where plasma neutrality was en-

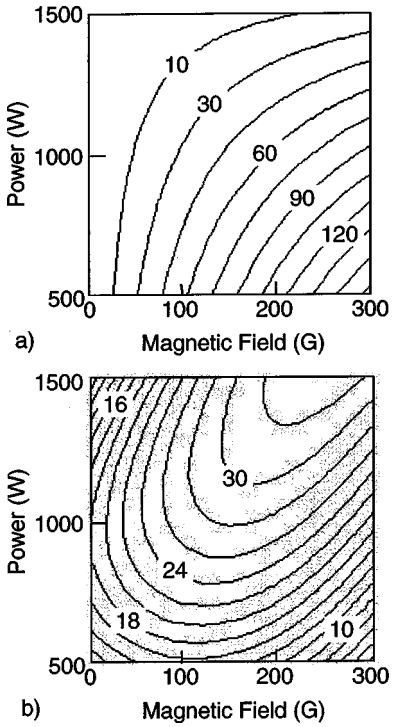

FIG. 17. Wavelength and uniformity scaling. (a) Static magnetic field divided by average electron density, β, as a function of magnetic field and power using an $Ar/Cl_2=80/20$ mixture. Wavelength scales with this quantity. The wavelength is large at high magnetic field and low power. (b) Uniformity parameter U for the ion flux to the substrate for the same conditions. The uniformity is worse for high values of U where the power deposition is directly above the substrate.

forced. An effective collision frequency for Landau damping was included. Results for an argon plasma in a solenoidal geometry showed the propagation of an electromagnetic wave which exhibits properties generally described by the dispersion relation of an $m=0$ mode. A resonant peak in the downstream plasma density occurring at low magnetic fields is attributed to off-resonant cyclotron heating. As the tube radius is decreased, this low field maximum in plasma density shifts toward higher magnetic fields. This result can be attributed to an increase in electron temperature and collision frequency as the tube radius is decreased, which tends to shift the power deposition efficiency to higher magnetic fields.

Results for a helicon plasma source sustained in Ar with an $m=0$ azimuthal antenna showed that as the magnetic field is increased to $\approx$100 G, electromagnetic field propagation in the axial direction dominates. Once the propagating wave encounters a boundary or intersects a counterpropagating wave (as in the radial direction), standing wave patterns may occur in the direction of propagation. Coincident in the axial propagation, power deposition and the peak in the plasma density shift downstream. A downstream shift in the peak plasma density also occurs in an Ar/Cl_2 gas mixture. However, unlike the pure Ar case, the plasma density shifts back upstream at 300 G. This shift upstream occurs due to the continual increase in the wavelength of the heliconlike wave as the static magnetic field is increased. At a high enough magnetic field, the wavelength is too large to sustain a standing wave pattern inside the chamber. If the plasma is significantly electronegative in the low power–high magnetic field regime, power deposition will resemble conventional ICP.

ACKNOWLEDGMENTS

This work was supported by the Semiconductor Research Corp., DARPA/AFOSR, National Science Foundation (CTS 99-74962), Applied Materials and LAM Research Corp.

[1]J. Perry and R. W. Boswell, Appl. Phys. Lett. **55**, 148 (1989).
[2]G. Perry, D. Vender, and R. W. Boswell, J. Vac. Sci. Technol. B **9**, 310 (1991).
[3]N. Jiwari, H. Iwasawa, A. Narai, H. Sakaue, H. Shindo, T. Shoji, and Y. Horike, Jpn. J. Appl. Phys., Part 1 **32**, 3019 (1993).
[4]F. F. Chen, J. Vac. Sci. Technol. A **10**, 1389 (1991).
[5]R. W. Boswell and F. F. Chen, IEEE Trans. Plasma Sci. **25**, 1229 (1997).
[6]F. F. Chen and R. W. Boswell, IEEE Trans. Plasma Sci. **25**, 1245 (1997).
[7]F. F. Chen, Phys. Plasmas **5**, 1239 (1998).
[8]D. Cheetham and J. P. Rayner, J. Vac. Sci. Technol. A **16**, 2777 (1998).
[9]J. P. Rayner and A. D. Cheetham, Plasma Sources Sci. Technol. **8**, 79 (1999).
[10]F. F. Chen, *Plasma Physics and Controlled Fusion* (Plenum, New York, 1984).
[11]A. Degeling, N. Mikhelson, R. W. Boswell, and N. Sageghi, Phys. Plasmas **5**, 572 (1998).
[12]F. F. Chen, Plasma Phys. Controlled Fusion **33**, 339 (1991).
[13]H. Gui and J. E. Scharer, IEEE International Conference on Plasma Science, 1999 (unpublished), p. 141.
[14]A. Degeling, J. E. Scharer, and R. W. Boswell, IEEE International Conference on Plasma Science, 2000 (unpublished), p. 226.
[15]F. F. Chen and D. D. Blackwell, Phys. Rev. Lett. **82**, 2677 (1999).
[16]J. G. Kwak, Phys. Plasmas **4**, 1463 (1997).
[17]W. Trivelpiece and R. W. Gould, J. Appl. Phys. **30**, 1784 (1959).
[18]K. P. Shamrai and V. B. Taranov, Plasma Sources Sci. Technol. **5**, 474 (1996).
[19]F. F. Chen and D. Arnush, Phys. Plasmas **4**, 3411 (1997).
[20]G. G. Borg and R. W. Boswell, Phys. Plasmas **5**, 564 (1998).
[21]D. G. Milak and F. F. Chen, Plasma Sources Sci. Technol. **7**, 61 (1998).
[22]R. L. Kinder and M. J. Kushner, J. Vac. Sci. Technol. A **17**, 2421 (1999).
[23]M. J. Grapperhaus and M. J. Kushner, J. Appl. Phys. **81**, 569 (1997).
[24]S. Rauf and M. J. Kushner, J. Appl. Phys. **81**, 5966 (1997).
[25]G. R. Tynan *et al.*, J. Vac. Sci. Technol. A **15**, 2885 (1997).
[26]W. H. Press, B. P. Flannery, S. A. Teukolsky, and W. T. Vetterling, *Numerical Recipes: The Art of Scientific Computing* (Cambridge University Press, Cambridge, 1986).
[27]M. A. Lieberman and A. J. Lichtenberg, *Principles of Plasma Discharges and Materials Processing* (Wiley, New York, 1994).
[28]P. L. G. Ventzek, M. Grapperhaus, and M. J. Kushner, J. Vac. Sci. Technol. B **12**, 3118 (1994).
[29]F. F. Chen, J. Vac. Sci. Technol. A **10**, 1389 (1992).
[30]PMT Corp. (unpublished).